Quasi-isothermal (Q-TG), cryoporometric (DSC) and adsorption characterization of activated carbons

Barbara Charmas[1] · Magdalena Zięzio[1] · Katarzyna Jedynak[2] · Karolina Kucio[1]

Abstract

In the presented paper, the structural and energetic heterogeneities of the activated carbons (ACs) surfaces were investigated. The ACs of well-developed microporosity were obtained from the spent coffee grounds as a result of pyrolysis (N_2 or CO_2) with the chemical activation of H_3PO_4 ($I = 1$, 1.5 or 2 w/w). The low-temperature N_2 adsorption, the quasi-isothermal thermogravimetry as well as the low-temperature differential scanning calorimetry were employed. Moreover, the selected materials adsorption properties were studied in relation to methylene blue (MB). The micro/mesoporous structure of the carbons was proved. The different types of water clusters on the surface indicated the carbons surface heterogeneity. The activated carbons are characterized by the high sorption capacity ($q_{e,exp} = 200.3$–237.67 mg g^{-1}) as for MB. The adsorption process was described by means of the Radke–Prausnitz isotherm model.

✉ Magdalena Zięzio
  magdalena.ziezio@poczta.umcs.lublin.pl

  Barbara Charmas
  barbara.charmas@mail.umcs.pl

  Katarzyna Jedynak
  kjedynak@ujk.edu.pl

  Karolina Kucio
  karolina.kucio@poczta.umcs.lublin.pl

[1] Faculty of Chemistry, Institute of Chemical Sciences, Maria Curie-Sklodowska University, Maria Curie-Sklodowska Sq. 3, 20-031 Lublin, Poland

[2] Institute of Chemistry, Jan Kochanowski University, Uniwersytecka Str. 7, 25-406 Kielce, Poland

Graphical abstract
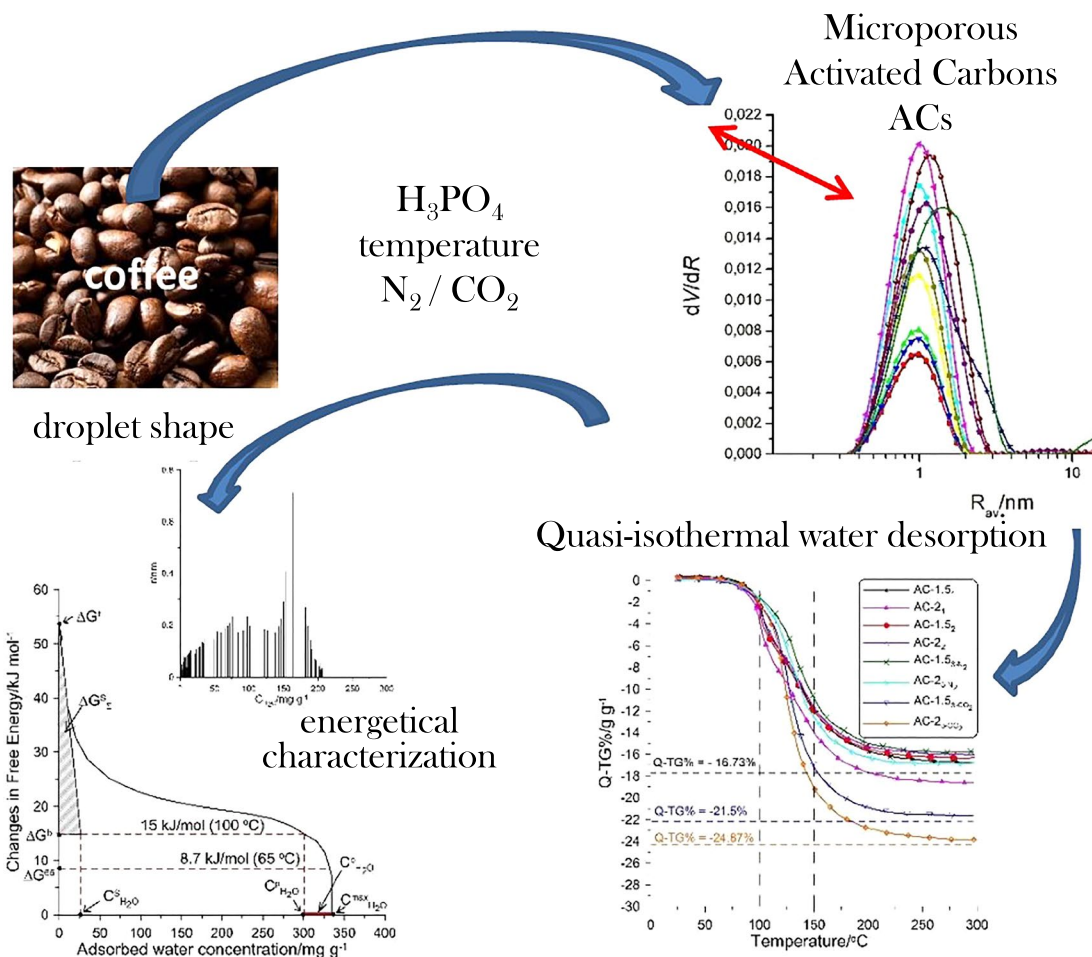
Introduction

An increase of population results in intense urbanization and industrialization growth, which entails the increase of the wastes, including those of organic origin. Such wastes are hazardous for ecosystems; thus, the reduction of the wastes and effective resource management become an essential issue [1, 2]. New, cheap and ecological methods of wastes management are needed. One of them is wastes processing into activated carbons leading to large reduction of wastes amount while obtaining materials capable of cleaning the natural environment which is in line with the principles of "green chemistry".

The waste sources used as precursors of organic matter are very numerous. Household wastes, such as unused parts of fruits [3, 4], coffee wastes [5, 6], sawdust and other wood processing wastes [7], energy-rich crops [8], textile [9] or food wastes [10, 11] and many others, account for their large amount. It should be also remembered that these wastes are characterized by a specific structure and porosity, which affects the properties of new materials to some extent. They are expected to be characterized by a large surface area, well-developed porous structure and specific functionalities, resulting in great sorption capacity. However, the materials originating from various wastes are characterized by the significant surface heterogeneity due to their origin, which also affects the adsorption properties of ACs.

The surface and structural heterogeneities of activated carbons can be assessed using thermal methods. Such methods include, for instance, thermogravimetric analysis under the quasi-isothermal conditions (Q-TG) and differential scanning calorimetry in the area of low temperatures (cryoporometry DSC). The Q-TG method is used to

analyze water (or other liquid) films adsorbed on the solids surface. The quasi-isothermal conditions enable controlling the temperature in such a way that the individual stages of liquid desorption, resulting from the different structure and surface chemistry of the solid (which causes differentiated interactions with the water molecules), proceed under constant temperature conditions [12–16]. This is the effect of different energy characteristics of the interactions at the carbon/liquid interface.

The dependence of the liquid molecules interactions strength on the structure and surface of a solid is also observed with the use of differential scanning calorimetry as the cryoporometric method. According to the Kelvin theory [17, 18], the behavior of a liquid during the phase changes in a limited space (in pores) is determined by the size of the pore radius and the possibility of interactions at the adsorbate/adsorbent interface related to the polarity of both media [19, 20]. The use of these methods results from the fact that water is constantly present in the surrounding atmosphere and is an active component of adsorption processes taking place in our environment. Therefore, it is necessary to get to know its positive or negative influence on the adsorption (e.g., of dyes) or chemisorption of gases and vapors as well as its potential influence on possible catalytic processes.

The aim of the paper was the characterization of the surface and structural heterogeneities of the activated carbons obtained from the household wastes (coffee wastes). The tests were carried out the using quasi-isothermal analysis (Q-TG) and low-temperature differential scanning calorimetry (DSC cryoporometry). The initial characteristics of the selected activated carbons were presented in [5, 21]. The results develop the knowledge of the water molecules interactions with the surface which leads to the assessment of the adsorption capacity of the tested materials. Therefore, the adsorption properties of the selected carbon materials in relation to methylene blue were also investigated.

Materials

The reagents used in this research were commercially available: H_3PO_4 (85 mass%; $d = 1.71$ g cm^{-3}; analytical grade; STANDARD, Poland), methylene blue (CHEMPUR, Poland).

Preparation of ACs

The spent coffee grounds (Arabica) from the households were used as a precursor. After washing with redistilled water and drying at 100 °C for 24 h, the raw material was fractionated and the 1–2 mm fraction was used in the studies. 100 g of the starting material was flooded with the appropriate amount of phosphoric acid ($I = 1$, 1.5 and 2 w/w ($m_{H3PO4}/m_{precursor}$); 85 mass%, $d = 1.71$ g cm^{-3}) diluted with redistilled water to the volume of 150 mL or 350 mL (Table 1). A larger amount of water (350 mL) was used for better penetration of the material by the impregnating agent. The prepared suspensions contained the amount of H_3PO_4 sufficient to obtain the assumed degree of impregnation. The suspensions were sonicated (3×10 min cycles) and placed on a shaker (30 °C/24 h/60 rpm). After 24 h before the pyrolysis process, a portion of the material was rinsed with a little amount of redistilled water (400 mL, procedures 1–3, Table 1) to remove the acid excess from the inter-particle spaces. The other part was left without washing off acid excess (procedures with the acid excess, 1-ex, 4-ex, Table 1). The impregnated materials were dried for 12 h at 100 °C.

Carbonization of the impregnated precursor

Carbonization of the impregnated materials was conducted according to the temperature programs presented in Table 1. The carbonization processes were run with the use of the multi-stage pyrolysis by introducing isothermal stages at

Table 1 Preparation procedure and scheme of the pyrolysis temperature programs

Procedure number	Preparation procedure	Pyrolysis temperature conditions	Sample designation
1	$V_{solution} = 350$ mL without acid excess	$20^oC \xrightarrow{10^oC/min} 800^oC(3h) \xrightarrow{cooling} 20^oC$	AC-1.5$_1$ AC-2$_1$
1-ex	$V_{solution} = 150$ mL with acid excess		AC-1$_{1-ex}$ AC-1.5$_{1-ex}$
2	$V_{solution} = 350$ mL without acid excess	$20^oC \xrightarrow{10^oC/min} 400^oC(1h) \xrightarrow{10^oC/min} 800^oC(3h) \xrightarrow{cooling} 20^oC$	AC-1.5$_2$ AC-2$_2$
3-N2	$V_{solution} = 150$ mL without acid excess	$20^oC \xrightarrow{10^oC/min} 400^oC(1h) \xrightarrow{10^oC/min} 800^oC(3h) \xrightarrow{cooling} 20^oC$	AC-1.5$_{3-N2}$ AC-2$_{3-N2}$
3-CO2			AC-1.5$_{3-CO2}$ AC-2$_{3-CO2}$
4-ex	$V_{solution} = 150$ mL with acid excess	$20^oC \xrightarrow{1^oC/min} 100^oC(5h) \xrightarrow{2^oC/min} 400^oC(1h) \xrightarrow{5^oC/min} 800^oC(3h) \xrightarrow{cooling} 20^oC$	AC-1.5$_{4-ex}$ AC-2$_{4-ex}$

$V_{solution}$ the total volume of the impregnation solution ($V_{acid} + V_{water}$), [mL]

selected temperatures to reduce the amount of by-products and to obtain the material with the developed surface. The processes took place in the N_2 atmosphere (flow rate 150 mL min^{-1}). Only in the case of 3-CO_2 procedure, in the sample annealing stage at the temperature of 800 °C, CO_2 was added as the oxidizing agent [5]. After the pyrolysis, the materials were washed with hot redistilled water to a neutral pH and dried for 12 h at 100 °C. The assay of the materials indicated a degree of impregnation (1, 1.5 or 2) and the number of the procedure (e.g., 1 or 1-ex and others). For example, the carbon designated AC-1.5$_{3-CO_2}$ was obtained from the coffee waste with the impregnation degree 1.5 using the 3-CO_2 procedure (Table 1).

Methods

Nitrogen adsorption/desorption

The materials textural characterization was made using the low-temperature (77.4 K, Micrometrics, ASAP 2405, Norcross, USA) nitrogen adsorption–desorption isotherms data. The specific surface area (S_{BET}) was calculated based on the standard BET method [22]. The nitrogen desorption data were used to compute the pore size distributions (PSD), differential $f_V(R) \sim dV_p/dR$ using a model of complex pores with the predominance of slit-shaped ones [23]. For the calculations, the SCR (self-consistent regularization) procedure under the non-negativity condition (f (R_p) > 0 at any pore radius R) was used. The value of the regularization parameter was $\alpha = 0.01$. The differential PSD curves with respect to the pore volume $f_V(R) \sim dV_p/dR$ were redefined as the incremental PSD (IPSD, $\sum \Phi_{v,i}(R) = V_p$). The $f_V(R)$ functions were also used to calculate contributions of micropores (V_{micro} and S_{micro} at $R \leq 1$ nm), mesopores (V_{meso} and S_{meso} at 1 nm < R < 25 nm) and macropores (V_{macro} and S_{macro} at $R > 25$ nm) to the total pore volume and the specific surface area. The total pore volume V_p was calculated as a sum of V_{micro}, V_{meso} and V_{macro} values. The Δw (the deviation from the assumed pore model) was calculated on the basis of the formula: (S_{BET}/S_{slit})–1 where S_{slit} is the specific surface area calculated with the assumed slit-shaped pore model; $S_{slit} = S_{micro} + S_{meso} + S_{macro}$ [23].

The elemental analysis

In order to conduct the elemental analysis, the analyzer CHNS EuroEA3000 (EuroVector) was employed. The hydrogen, carbon, nitrogen and oxygen contents (%) were determined.

Quasi-isothermal water desorption

The water vapor was adsorbed on the carbons surface at 25 °C. Two grams of each sample was placed in the desiccator with the bidistilled water for 72 h. Then, the weighed portions (~ 50 mg) of the saturated materials were placed in a spiral platinum crucible. The thermodesorption of water under the quasi-isothermal conditions was performed using the Derivatograph C (Paulik, Paulik and Erdey, MOM, Hungary). On the basis of the obtained results, there were determined the values characterizing the tested materials: the total amount of adsorbed water (TG^{max}), the amount of weakly (TG^w) and strongly (TG^s) bound water, the surface free energy at the adsorbent/water interface as well as the number of statistical water monolayers [24–26]. The calculation procedures are included in the SI.

Low-temperature differential scanning calorimetry (cryoporometry DSC)

The calorimetric studies (DSC) were carried out with the differential scanning calorimeter (DSC PYRIS Diamond, Perkin Elmer, USA). The temperature calibration was performed using the redistilled water ($T_m = 0$ °C) and the indium standard ($T_m = 156.6$ °C). The ice melting curves (from −120 °C to 20 °C, 2 °C min^{-1}) were used to determine the PSD$_v$ curves. The tests were carried out after the first freezing because according to reports [27] formation of ice crystals during the water freezing in the pores causes the increase of R and V of mesopores. Therefore, when using water as a medium, it is recommended to conduct an analysis based on the DSC curves from the first measurement. This remark applies especially to the materials with a delicate structure, including carbon materials. Before testing, the samples were saturated with water vapor in the desiccator (25 °C, 72 h). The degree of water saturation was determined from the thermogravimetric measurements (Q-TG). The weighed samples (~ 5 mg) were sealed in the aluminum pans. The reference sample was an empty aluminum crucible. The research was carried out in the inert gas atmosphere—helium. Nitrogen was used as the curtain gas.

During the DSC data analysis, the thickness of the non-freezing water layer was taken into account (0.8 nm [28]) corresponding to the three water statistic monolayers [29]. On the basis of the DSC curves of ice melting, the transition temperatures (T_{onset}), the temperatures at which the ice melting rate was the highest (T_{max}), the pore radius and the dV/dR dependencies have been determined. The calculation procedures are included in the SI.

Raman spectroscopy

The Raman spectroscopy investigations were carried out by means of inVia Reflex (Renishaw, UK) with the Raman dispersive system using the 514 nm argon laser. The application of 1.4 mW of laser power prevented from sample overheating.

Kinetic studies

In the adsorption studies, the batch method was applied. The kinetic investigations were carried out at the temperature of 30 °C. Methylene blue (MB, $C_0 = 700$ mg L^{-1}) was used as the model contaminant. The previously prepared solutions (0.025 L) were added to the conical flasks which contained the appropriate amount of adsorbent (0.05 g). The flasks with the solution and activated carbon were placed on a shaker (75 rpm, 222 h). Changes in the dye concentration at the specified intervals were evaluated using a UV–VIS spectrophotometer ("Helios Gamma", Spectro-Lab, Poland) at the wavelength of 664 nm. In the paper, the kinetic process in the solid–liquid system is described by the pseudo-first-order equation, the pseudo-second-order equation, the Elovich kinetic model as well as the intra-particle diffusion model [30]. The calculation procedures are included in the SI.

Determination of adsorption isotherms

For determination of the adsorption isotherms, the MB solutions of the appropriate concentrations (300–1000 mg L^{-1}) were used. The specified amounts (0.05 g each) of activated carbon were placed in the Erlenmeyer flasks, and then, the MB solutions were added. Next, they were put on the shaker (30 °C, 75 rpm). After 130 h (the time required to reach the adsorption equilibrium at saturation), the solutions concentrations were measured. The Langmuir, Freundlich and Radke–Prausnitz adsorption isotherms models were used to determine the basic parameters of the adsorption process [31, 32]. The calculation procedures are included in the SI.

Moreover, the average absolute percentage deviation (%Dev) was calculated. This value indicates the difference between the q_e values obtained on the basis of the studies. ($q_{e,exp}$) and the predicted values ($q_{e, pred}$) [33]:

$$\%\text{Dev} = \left(\frac{1}{N} \sum_{i=1}^{N} \left| \frac{q_{e,exp} - q_{pred}}{q_{e,exp}} \right| \right) \cdot \leq 100\%$$

Moreover, the standard deviation was calculated.

Results and discussion

Structural characteristics

The elemental composition of the starting material and activated carbons is presented in Table SI 1 (Supplementary Information). The starting material (SCGs) is characterized by relatively high hydrogen (8.08%), oxygen (39.85%) and carbon (49.87%) contents. This indicates that SCGs are an appropriate source of carbon matter for preparation of carbon adsorbents. For all obtained ACs, the contents of hydrogen (1.64–2.64%), oxygen (28.98–35.87%), nitrogen

Table 2 Structural characteristics of the carbons

Sample	S_{BET}	S_{micro}	$\%S_{micro}$	S_{meso}	$\%S_{meso}$	V_p	V_{micro}	$\%V_{micro}$	V_{meso}	$\%V_{meso}$	V_{macro}	$\%V_{macro}$	R_{av}	Δw
AC-1.5$_1$	216.2	170.4	78.8	45.9	21.2	0.101	0.069	68.3	0.032	31.7	0	0	0.92	0.996
AC-2$_1$	219.3	173.4	79.0	46.0	21.0	0.102	0.07	68.7	0.032	31.3	0	0	0.93	0.948
AC-1.5$_2$	273.9	215.5	78.7	58.4	21.3	0.126	0.086	68.1	0.04	31.9	0	0	1.43	0.966
AC-2$_2$	255.5	199.7	78.2	58.8	21.8	0.117	0.079	66.9	0.038	32.3	0	0	1.47	0.110
AC-1.5$_{3-N2}$	400.5	312.3	78.0	88.2	22.0	0.148	0.123	66.8	0.06	32.7	0.001	0.5	1.39	0.354
AC-2$_{3-N2}$	464.2	356.1	76.7	108.1	23.3	0.212	0.138	65	0.073	34.4	0.001	0.5	1.4	0.294
AC-1.5$_{3-CO2}$	614.8	469.1	76.3	145.6	23.7	0.284	0.182	64	0.099	34.8	0.003	1.1	1.5	0.232
AC-2$_{3-CO2}$	720.9	536.9	74.5	184.1	25.5	0.334	0.206	61.7	0.126	37.8	0.002	0.6	1.5	0.295
AC-1$_{1-ex}$	543.3	346.7	63.8	196.6	36.2	0.292	0.131	45	0.161	55	0	0	1.8	0.514
AC-1.5$_{1-ex}$	619.8	408.6	65.9	211.0	34.0	0.306	0.152	49.6	0.15	49	0.004	1.4	1.83	0.145
AC-1.5$_{4-ex}$	727.8	455.0	62.5	272.8	37.5	0.367	0.17	46.3	0.196	53.5	0.001	0.2	1.4	0.509
AC-2$_{4-ex}$	632.6	329.7	52.1	302.9	47.9	0.378	0.124	32.7	0.254	63.7	0	0	1.9	0.356

S_{BET}—the specific surface area [m^2 g^{-1}]; S_{micro}—the micropores surface [m^2 g^{-1}]; $\%S_{micro}$—the share of micropores area [%] (S_{micro}/S_{BET}) *100%; S_{meso}—the mesopores surface [m^2 g^{-1}]; $\%S_{meso}$—the share of mesopores area [%] (S_{meso}/S_{BET}) *100%; V_p—the pore volume determined as the sum of the micro-, meso- and macropores volumes [cm^3 g^{-1}]; $\%V_{micro}$—the share of micropores volume [%] (V_{micro}/V_p)*100%; $\%V_{meso}$—the share of mesopores volume [%] (V_{meso}/V_p)*100%; V_{macro}—the macropores volume [cm^3 g^{-1}]; $\%V_{macro}$—the share of macropores volume [%] (V_{macro}/V_p)*100%; R_{av}—the average pore radius; Δw—the deviation from the assumed pore model
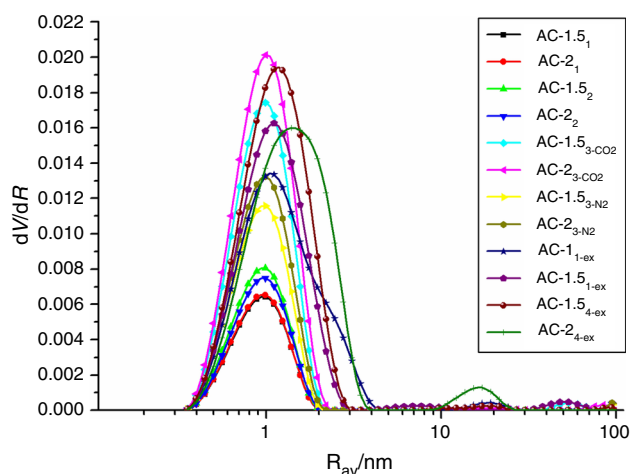
Fig. 1 Pore volume distribution curves for the activated carbons

(2.10–2.78%) and carbon (59.61–66.30%) are very similar. That is why one can assume that the impregnation ratios as well as the pyrolysis procedures did not have a significant effect on the elemental composition.

Table 2 shows the structural parameters of the tested materials. The data analysis proves that these materials have a fairly well-developed surface area and pore volume. They are characterized mainly by the micro/mesoporous structure.

As follows from the presented data, the percentage of the micropore area ($\%S_{micro}$) in the materials obtained according to the procedures without the acid excess (procedures 1–3) is approx. 75–79% (share of the micropore volume $\%V_{micro}$ is c.a. 62–69%). The average pore radius (R_{av}) of these materials is about 0.9–1.5 nm (Table 2). The obtained data indicate very small macropore contents. A slightly smaller proportion of micropores is found in the case of the materials pyrolyzed in the presence of H_3PO_4 excess. The shares of the micropores area are ~52.1–65.9%. ($\%V_{micro}$ is below 50%.)

Figure 1 shows the curves of the pore volume distribution in relation to their mean radii for the tested carbons. One can see the clearly developed maximum in the range of R_{av} values presented in Table 2. There are also the peaks indicating the presence of small amounts of meso- and macropores. The presented peaks are quite wide; however, the PSD_v distributions show the monomodal character of the pores. The small values of Δw (Table 2) indicate a good adjustment of the assumed pore model.

A significant content of micropores favors the adsorption properties of the tested carbon materials; therefore, a thorough characterization is desirable, especially in terms of hydrophilic properties and the possibility of interactions of water molecules (as a common solvent).

Quasi-isothermal analysis

The results of water thermodesorption (Q-TG%) under the quasi-isothermal conditions for the activated carbons are presented in Fig. 2. The slight inflection points correspond to the consecutive stages of water evaporation in different energetic states. The differentiated energetic stages of water are due to various interactions with the carbon surface [34]. The first is unbound (free, strongly associated) water located in wide mesopores and macropores. Such molecules do not interact with the pores walls and are characterized by the bulk water properties. The second type is weakly bound water which is characterized by weak interactions with the solid surface and freezes (DSC) at the temperatures slightly below 0 °C but evaporates (Q-TG) at a little over the boiling point (100 °C). The third type is strongly bound water which interacts strongly with the solid surface through hydrogen bonds or electrostatic interactions, especially with the participation of surface functionalities. Strongly bound water in the micropores remains unfrozen at about $T < -15$ °C or is desorbed from the carbon surface at a temperature higher than the boiling point of weakly bound water [35] because of strong interactions of water molecules and surface functionalities or heteroatoms. Weakly and strongly bound water can be in the form of large aggregates or clusters located on the polar/non-polar surfaces. The contributions of the different forms of water depend on the pore structure and surface chemistry of the pore walls. Thus, water thermodesorption took place not exponentially but gradually. This points out to the change in the properties of the water layer depending on the distance from the solid surface.

During the thermodesorption under the quasi-isothermal conditions to the temperature of ~100 °C, the liquid excess outside the adsorbent pores (i.e., physically bound water or bulk water) evaporates. Due to the interactions between the adsorbate and the ACs surface, water desorption takes place in the pores at higher temperatures. As the materials were pre-saturated with the water vapor (72 h, 25 °C), they contained a minimum amount of moisture which was desorbed at 100–105 °C (Fig. 2a, b). Table 3 presents the characteristics of the adsorbed water layers. The values of TG^w (experimental data) and C^b_{H2O} (calculated data) represent the concentrations of physically bound water which constitutes about 10–15% of the total adsorbed water (TG^{300}_{max}; C^{max}_{H2O}). These values are characterized by great compliance (Table 3).

The course of the analyzed curves (Fig. 2a,b) in the second stage shows that the total mass loss in the temperature range from 100 to 300 °C is greater for the 1-ex and 4-ex procedures (Fig. 2b). For example, for the AC-1.5₁ sample the maximum Q-TG% mass loss is 16.7%, while for the AC-1.5₁-ex it is 22.1%. This suggests that the use of the procedures with the acid excess results in obtaining materials

with a better developed surface which is consistent with the structural data presented in Table 2.

The analysis of the curves (Fig. 2) for the AC-1.5$_1$ and AC-1.5$_{1\text{-ex}}$ samples indicates a greater mass loss observed for the materials obtained according to the excessive procedure and is related to the larger pore size in this material (AC-1.5$_{1\text{-ex}}$). Such observations are consistent with the data obtained from the N$_2$ adsorption (Table 2) which shows that owing to the excessive procedures materials with a significant content of mesopores are obtained.

The Q-TG analysis indicates better surface development with the extended pyrolysis stages. The maximum Q-TG^{300} mass loss for the sample obtained according to the 4-ex procedure is the largest of the tested materials (e.g., AC-2$_{4\text{-ex}}$ sample, Q-TG% = 27.4%) and confirms its greatest porosity (V_p = 0.378 cm^3 g^{-1}, Table 2). A positive effect of developing a porous structure is also indicated by the Q-TG curves for the materials pyrolyzed in the CO$_2$ atmosphere (AC-1.5$_{3\text{-CO2}}$ and AC-2$_{3\text{-CO2}}$). In the series of the materials obtained based on the procedures without the acid excess (Fig. 2a), these materials are characterized by the largest mass loss of the water adsorbed inside the pores (Table 3).

Various stages of water thermodesorption are clearly visible on the Q-DTG curves (Fig. 2c, d) where the fundamental differences in the curves course can be seen. In the first step at a high degree of surface hydration, all pores remain filled with water and only the bulk water (moisture) is evolved. Such an effect can be seen for the samples from procedures 1 and 2 at the temperature of ~100 °C (Fig. 2c). At this temperature, the water evaporates at the water/air interface. The second stage of water mass loss occurs at a higher temperature and is associated with the water desorption from the pores. This effect is found for the carbons prepared according to the procedures with the acid excess (procedures 1-ex and 4-ex; Fig. 2d) as well as procedure 3 (Fig. 2c). The shift of temperature at which water desorption is the fastest results from the different porosity of the materials. The carbons obtained according to procedure 3 have a larger share of micropores (e.g., AC-2$_{3\text{-N2}}$, %V_{micro} ~ 65%, Table 2) and smaller sizes (R_{av} ~ 1.4 nm, T$_{\text{Q-DTG}}$ = 122 °C, Fig. 2c) than the materials obtained according to the procedures with the acid excess (e.g., AC-2$_{4\text{-ex}}$, %V_{micro} = ~ 33%, R_{av} ~ 1.9 nm, Table 2); therefore, the water desorption from the latter takes place at a lower temperature (T$_{\text{Q-DTG}}$ = 118 °C, Fig. 2d).

Figure 2e shows the dependence of the change in the free energy (ΔG) of water as a function of its concentration (C$_{\text{H2O}}$) on the surface for the exemplary AC-2$_{3\text{-CO2}}$ sample. For all obtained materials, these dependencies $\Delta G = f(\text{C}_{\text{H2O}})$ have a similar course. In the first stage of the water desorption process (high values of adsorbed water concentration), the water concentration changes are small and do not exceed 15% of the initial adsorbed water concentration (Fig. 2e, the bulk water, C$_{\text{H2O}}^b$). After reaching the temperature

corresponding to the boiling point of the water contained in the pores ($\Delta G^b = G - G_0 = 15$ kJ mol^{-1}; 100 °C), desorption of the more strongly adsorbed water begins.

The water evaporation started at $\Delta G^{65} = 8.7$ kJ mol^{-1} ($T = 65$ °C). The total desorption process took place in a relatively wide temperature range (Fig. 2a, b) due to the microporous nature of the carbons. With the temperature increase, the adsorbed water remained only in the micropores in the form of thin layers or clusters. A further increase in the temperature caused the thermodesorption of water bound directly to the adsorbent surface (the so-called strongly bound water, C$_{\text{H2O}}^s$). On the basis of the dependence $\Delta G = f(\text{C}_{\text{H2O}})$ (Fig. 2e), the values of the total surface free energy at the adsorbent/water interface were determined (Table 3, ΔG_{Σ}). Parts of the area corresponding to the low concentrations of adsorbed water (highlighted grey triangle, Fig. 2e) were used to calculate the surface free energy at the adsorbent/strongly bound water interface (Table 3, ΔG_{Σ}^s).

Table 3 presents the characteristics of the water layers adsorbed on the surface of the tested activated carbons. A great compliance of the parameters obtained directly from the TG% (Fig. 2a, b) (TG$_{\text{max}}^{300}$, TG^w, TG^s) with the calculated values using the equations Eqs SI 1–SI 3 is observed. An increase in the maximum concentration of the adsorbed water (C$_{\text{H2O}}^{\text{max}}$) was found with the increasing impregnation ratio. For the materials prepared based on the 1-ex and 4-ex procedures, these values are much higher compared to those of the remaining carbons because they are characterized by a much better developed surface and porosity (Table 2) exhibiting better sorption properties. In the case of strongly adsorbed water concentration, C$_{\text{H2O}}^s$, an inverse relationship is found. Its values decrease with the increasing impregnation degree.

Table 3 presents the values of the total surface free energy at the adsorbent/water interface (ΔG_{Σ}) and the surface free energy at the adsorbent/strongly bound water interface (ΔG_{Σ}^s). The highest values of the discussed parameters were determined for the materials with the least developed surface (procedures 1 and 2).

Figure 3a–c shows the dependence of the effective radius of the evaporating droplet on the adsorbed water concentration for the selected adsorbents (AC-1.5$_1$, AC-1.5$_{3\text{-N2}}$, AC-1.5$_{4\text{-ex}}$). It is assumed that the size of the evaporating droplet depends on the pore size of the tested material. For most of the carbons, the evaporating water droplet size distribution has a bell shape and corresponds to the Gaussian type model (Fig. 3b). However, in some cases (carbons obtained according to procedure 1) the obtained profiles differ from the Gaussian model (AC-1.5$_1$ Fig. 3a). In the above cases, there can be observed 2 maxima on the evaporating droplet size distribution curves indicating a biporous structure of the tested carbon. This was also demonstrated on the Q-TG
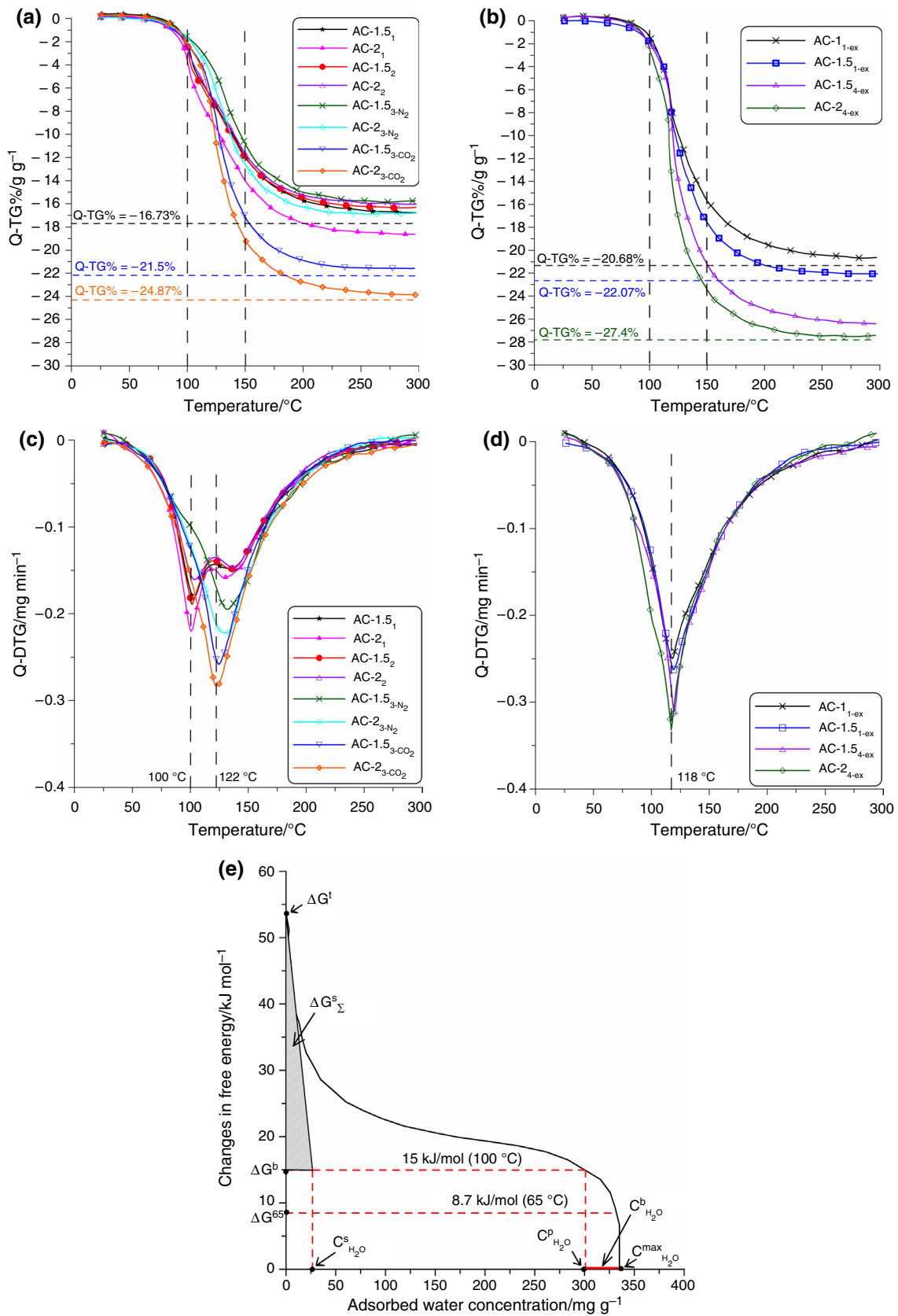
◄**Fig. 2** Course of the curves Q-TG% (**a, b**) and Q-DTG (**c, d**) for the materials obtained according to the procedures without the acid excess (**a, c**) and with the acid excess (**b, d**) under the quasi-isothermal conditions and the dependence of the changes of ΔG value on the concentration of adsorbed water for the exemplary AC-$2_{3\text{-}CO_2}$ sample (**e**)

(Fig. 2a) and Q-DTG (Fig. 2c) curves. The shape of the curves in question indicates that in the initial stage of water thermodesorption (low temperature, high C_{H2O}) the effective radius of the evaporating droplet is small, and with a decrease in the water concentration (with the increasing temperature), it increases to the value determining the radius of the dominating pores (R_{dom}). A further temperature increase causes a decrease in the concentration of the adsorbed water and a decrease in the size of the effective radius of the evaporating droplet.

Figure 3d–f presents the dependence of dG/dM as a function of the number of water statistical monolayers (n) under the conditions of small water coverage where dG/dM indicates the change in the free energy of the system during the water evaporation from the surface. In the area of low water saturation, there are 1 to 3 statistical monolayers of water filling the micropores on the surface of the materials [36]. There can be observed numerous maxima in the presented relationships (e.g., the inset in Fig. 3d–f), pointing out to the formation of various water clusters on the heterogeneous surface of the tested activated carbons [24].

Cryoporometry DSC

The porous structure of the obtained activated carbons was also determined using the low-temperature DSC as a cryoporometric method. The DSC cryoporometry is based on the phenomenon of decreasing the liquid freezing point (in this case: the water) as a result of its entrapment in the pores of the tested materials. The theory assumptions and the relationships are presented in the SI (Eqs SI 4–SI 7).

The degree of pore filling by media of different polarities depends on the nature of the surface of the tested material and is related to its porosity [37]. It was assumed that ice melts in the narrowest pores (R_{min}) at T_{onset}, while the T_{max} corresponds to the water melting in the pores of the average size (R_{av}). The characteristic ice melting points in the tested materials are given in Table 4.

The analysis of the obtained DSC curves indicates a multi-stage course of the ice melting process. There are observed shifts of characteristic temperatures (T_{onset}) toward smaller values with an increase in the impregnation degree and an extension of the pyrolysis process time (except for the 3-CO_2 and 4-ex procedures). Moreover, a decrease in the melting point of the ice contained in the pores (in the range −3.99 to −5.65 °C) in relation to the melting point of the

volumetric ice (0 °C) (Table 4) can be seen. The reduction of ice melting temperature is a result of the interactions of water with the surface of narrow pores of the tested materials (Table 2).

Figure 4a, b shows the curves of pore volume distribution in relation to their mean radii obtained from the ice melting curves. The δ layer thickness (0.8 nm) was taken into account in the calculations. Cryoporometry tests using water showed that the investigated ACs are characterized by a narrow pore size distribution and the value of the dominant radius is about 1.1 nm. Such values are close to the results presented in Table 2, although due to the different specificity of the used methods there is no complete agreement. The observed trends of changes in the height of the discussed curves confirm the increase in the volume of micropores with the increasing degree of impregnation (Fig. 4).

Raman spectroscopy

The Raman spectra obtained for the selected activated carbons are given in Fig. 5. The position and shape of the spectrum, ascribed to the specific form of carbon, provide the information about the structures (i.e., crystalline, nanocrystalline or amorphous) in a given material [38]. In the case of activated carbons, one can observe two characteristic bands: a wider D-band (~ 1360 cm^{-1}) attributed to the disordered carbon and a narrower G-band (~ 1580 cm^{-1}) corresponding to the graphite domains [39]. In order to analyze the obtained materials, the ratio of the D and G I_D/I_G bands intensity is also determined indicating the graphitization degree. It is assumed that the I_D/I_G ratio 0.85–1.00 indicates the non-graphitic nature of activated carbons [40, 41].

In the presented spectra (Fig. 5), a significant increase in the intensity of the D and G bands for the AC-$2_{4\text{-ex}}$ sample compared to the other materials can be found. This effect may be due to the use of acid excess procedures and the introduction of isothermal intermediate stage during the pyrolysis process. No significant changes were observed in the position of the G bands which determines the type of carbon material structure (Fig. 5). The I_D/I_G band intensity ratio is in the range 0.92–0.96 (Fig. 5) which may indicate a largely disordered graphene structures with a significant sp^3 content. The obtained results indicate the non-graphitic, i.e., amorphous nature of carbons.

Kinetic studies

The research on the possibility of using the obtained activated carbons in the process of dye adsorption was carried out with the use of the best developed surface materials (AC-$1.5_{3\text{-}CO_2}$ and AC-$2_{3\text{-}CO2}$).

Figure 6a shows the kinetics of the methylene blue adsorption process for the two tested activated carbons,

Table 3 Characteristics of the adsorbed water layers on the surface of ACs

Sample	TG_{max}^{300}	TQ^w	TQ^w	C_{H2O}^{max}	C_{H2O}^b	C_{H2O}^p	C_{H2O}^s	ΔG_Σ	ΔG_Σ^s	n_{H2O}
AC-1.5$_1$	202	24	178	205.3	28.1	177.3	15.5	683.6	366.7	2.62
AC-2$_1$	229	49	180	229.8	47.7	182.1	18.6	699.9	357.3	2.88
AC-1.5$_2$	194	32	162	197.1	39.5	157.6	11.5	490.9	252.4	1.97
AC-2$_2$	190	31	159	191.5	37.5	154.0	11.1	523.7	276.6	2.06
AC-1.5$_{3-N2}$	187	19	168	188.6	19.3	169.2	16.6	360.6	203.1	1.30
AC-2$_{3-N2}$	203	24	179	199.8	19.8	179.9	7.5	306.8	161.4	1.18
AC-1.5$_{3-CO2}$	275	36	239	276.7	31.1	245.5	12.7	310.1	160.1	1.23
AC-2$_{3-CO2}$	330	31	299	334.9	34.9	300.0	26.3	329.6	173.2	1.27
AC-1$_{1-ex}$	260	39	221	261.6	19.8	241.8	15.4	349.2	184.0	1.32
AC-1.5$_{1-ex}$	283	62	221	283.1	23.0	260.0	13.8	315.2	161.1	1.26
AC-1.5$_{4-ex}$	364	42	322	362.9	29.8	333.1	26.3	350.4	180.9	1.37
AC-2$_{4-ex}$	377	57	320	379.9	43.3	336.6	18.1	374.3	169.7	1.65

TG_{max}^{300}—the total amount of adsorbed water [mg g^{-1}]; TG^w—the amount of weakly adsorbed water [mg g^{-1}]; TG^s—the amount of strongly adsorbed water [mg g^{-1}]; C_{H2O}^{max}—the maximum concentration of adsorbed water [mg g^{-1}]; C_{H2O}^b—the bulk water concentration [mg g^{-1}]; C_{H2O}^p—the water concentration in all types of pores [mg g^{-1}]; C_{H2O}^s—the strongly adsorbed water concentration (in micropores) [mg g^{-1}]; ΔG_Σ—the total surface free energy at the adsorbent/water interface [mJ m^{-2}]; ΔG_Σ^S—the surface free energy at the adsorbent/strongly bound water interface [mJ m^{-2}]; n_{H2O}—the number of statistical monolayers of water
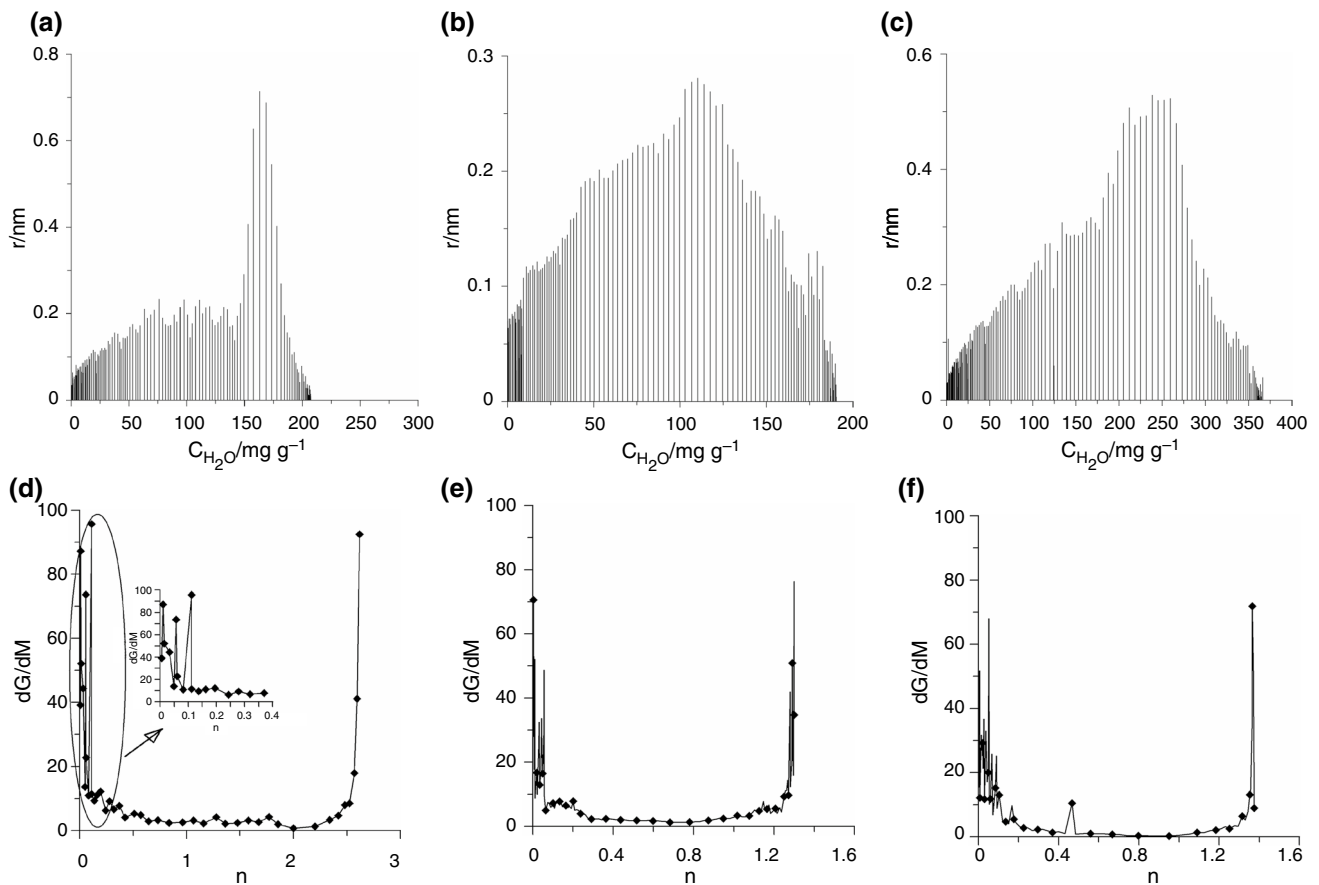

Fig. 3 Dependence of the effective radius of the evaporating droplet on the concentration of the adsorbed water for the materials AC-1.5$_1$ (**a**), AC-1.5$_{3-N2}$ (**b**) and AC-1.5$_{4-ex}$ (**c**) as well as the dependence of dG/dM under the conditions of small surface filling with the adsorbed water for the materials AC-1.5$_1$ (**d**), AC-1.5$_{3-N2}$ (**e**) and AC-1.5$_{4-ex}$ (**f**)

Table 4 Characteristic ice melting points determined on the basis of DSC curves of the tested adsorbents

Sample	T_{onset}	T_{max}
AC-1.5$_1$	−4.49	−2.82
AC-2$_1$	−5.38	−3.79
AC-1.5$_2$	−5.44	−3.83
AC-2$_2$	−5.84	−4.09
AC-1.5$_{3-N2}$	−4.76	−3.18
AC-2$_{3-N2}$	−5.16	−3.56
AC-1.5$_{3-CO2}$	−4.37	−2.92
AC-2$_{3-CO2}$	−3.99	−2.55
AC-1$_{1-ex}$	−4.91	−3.28
AC-1.5$_{1-ex}$	−5.40	−3.28
AC-1.5$_{4-ex}$	−5.65	−3.79
AC-2$_{4-ex}$	−4.10	−3.60

T_{onset} the temperature of the phase transition origin [°C]; T_{max} the temperature at which the transformation occurs fastest [°C]

i.e., AC-1.5$_{3-CO2}$ and AC-2$_{3-CO2}$. As can be seen in the initial stage (about 20 h) the dye adsorption on both tested materials was very intensive. However, due to the fact that the tested materials contain mainly micropores (AC-1.5$_{3-CO2}$%S$_{micro}$ = 76.3 and AC-2$_{3-CO2}$%S$_{micro}$ = 74.5; Table 2), the equilibrium state was achieved after about 130 h.

For better understanding of the kinetics of methylene blue adsorption on the tested materials, kinetic parameters were determined for the pseudo-first and pseudo-second-order kinetic models using the linear relationships (SI, Eqs SI 8 and SI 9). The determined parameters are presented in Table 5a. The obtained results indicate that in the case of PFO the calculated $q_{e, calc}$ ones are much closer to the experimental $q_{e, exp}$ values than the $q_{e, calc}$ values determined from the pseudo-second order equation. However, the correlation coefficient R^2 for both materials reaches higher values for the

pseudo-second order model ($R^2 = 0.96$–0.99). Thus, it can be concluded that the pseudo-second order model describes the kinetics of methylene blue adsorption on the tested activated carbons better.

The tested adsorbents were assumed to be characterized by the energetic heterogeneity which means that there are active centers with different binding strengths of the dye molecules on their surface. The chemisorption process can also take place on this type of surface [42, 43]. Therefore, the Elovich kinetic model (SI, Eq. SI 10) was applied. As follows from the results presented in Table 4a, large values of the correlation coefficient $R^2 = 0.90$ for AC-1.5$_{3-CO2}$ and $R^2 = 0.94$ for AC-2$_{3-CO2}$ (Table 5a) prove that the adsorption rate is also affected by the chemisorption process. However, the experimental data (Table 5a) indicate clearly a much better fitting with the pseudo-second order kinetic model.

In order to investigate the mechanism controlling the kinetics of the dye adsorption process, the intra-particle diffusion model proposed by Weber-Morris [42] was used.

Figure 6b shows the relationship q_t versus $t^{1/2}$, while Table 5b contains the parameters determined using the linear relationships (SI, Eq. SI 11). As can be seen in Fig. 6b, the multi-line relationships were obtained for both tested carbons, indicating the presence of three stages. The first stage is very fast and intense involving the dye adsorption on the active sites located on the adsorbent outer surface. The second stage is slower compared to the first one and is related to the intra-particle diffusion of methylene blue molecules in the pores of activated carbons. In turn, the third stage indicates clearly the state of equilibrium in which the intra-particle diffusion rate decreased significantly which might result from a very small concentration of the dye remaining in the solution [44], fewer accessible active sites [45] as well as the transfer of dye molecules from larger pores to the micropores [46]. These observations are confirmed by the data presented in Table 5b. The obtained results show that for each successive stage the

Fig. 4 Curves of pore volume distribution against their mean radii for the materials obtained according to the procedures without (**a**) and with (**b**) the acid excess obtained by the analysis of the ice melting curves
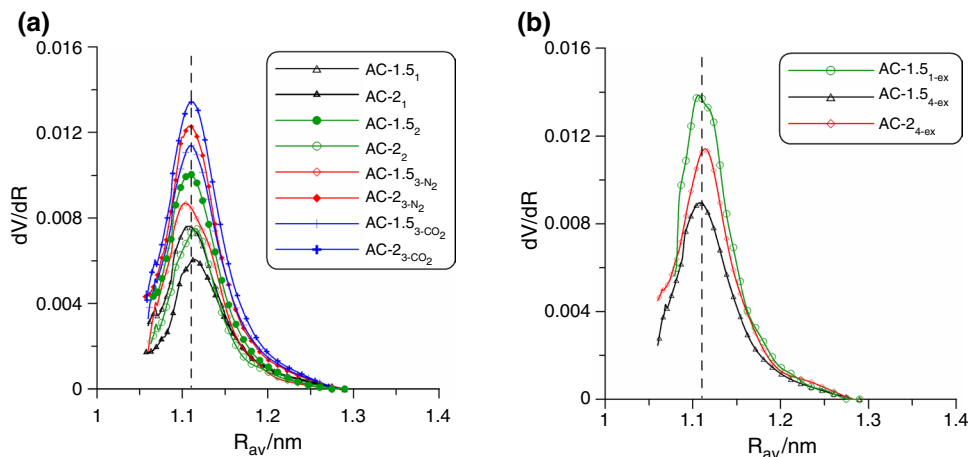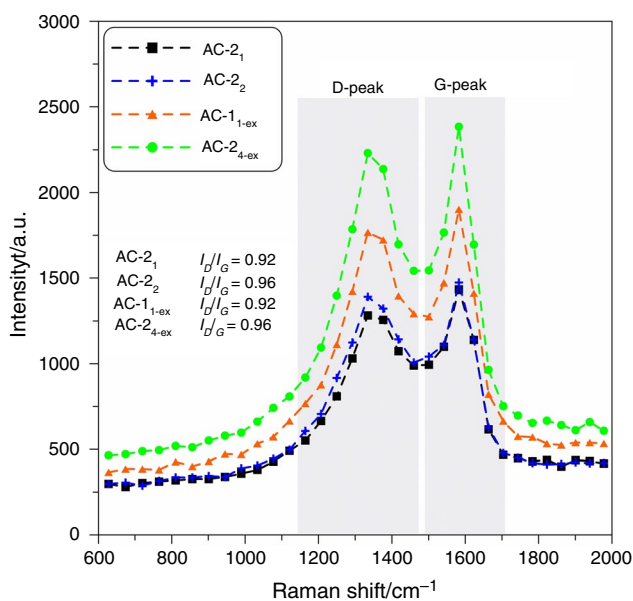
Fig. 5 Raman spectra of the selected activated carbons

values of the rate constants (k_d) decrease: $k_{d1} > k_{d2} > k_{d3}$. This effect is particularly visible in the case of the AC-$2_{3\text{-}CO2}$ sample where the k_d values were: $k_{d1} = 50.80 > k_{d2} = 29.16 > k_{d3} = 3.64$, respectively. Moreover, there were obtained very high values of the R^2 correlation coefficient ($R^2 > 0.95$; Tab. 5b), which is characteristic of a linear fit for the second stage of the relationship $q_t = f(t^{1/2})$. Furthermore, the C values obtained in each case were different from zero. From above observations and conclusions, it was found that the intra-particle diffusion plays an important role in the process of methylene blue adsorption on the tested activated carbons, but this is not a step determining the speed of the entire process.

Adsorption isotherms

Figure 6c, d presents the adsorption isotherms. As can be seen for both materials, the adsorption capacities increase with the increasing concentration of methylene blue, while they achieve the plateau at high dye concentrations. The maximum sorption capacity calculated from the experimental data (SI, Eq. SI 12) is 200.30 mg g^{-1} for the AC-$1.5_{3\text{-}CO2}$ sample (Fig. 6d) and $q_{e,exp} = 237.67$ mg g^{-1} for the AC-$2_{3\text{-}CO2}$ sample (Fig. 6d).

Compared to the AC-$1.5_{3\text{-}CO2}$ material, the sorption capacity of AC-$2_{3\text{-}CO2}$ carbon is greater because it has a much better developed structure and a larger pore volume (Table 2; Fig. 1). Moreover, this difference is assumed to be due to the different number of accessible active centers.

AC-$2_{3\text{-}CO2}$ carbon is characterized by a higher impregnation ratio and thus probably contains more phosphorus atoms in its structure. According to Puziy et al. [47], heteroatoms give the carbons specific adsorption properties. The phosphorus-containing carbon materials have a large adsorption capacity toward metal ions and organic molecules. Additionally, heteroatoms such as phosphorus can also act as the additional adsorption centers capable of binding the dye molecules.

The determination of the appropriate type of adsorption isotherm is important to describe the manner of the adsorbed molecules arrangement and interactions with the adsorbents. In the paper, both the Langmuir and Freundlich bi-parameter models as well as the Radke–Prausnitz three-parameter model were applied (Fig. 6c, d). The nonlinear forms of the equations Eqs SI 13–SI 15 were used.

Table 6 shows the calculated values of the variables in the nonlinear forms of the isotherm models. In the case of the Langmuir isotherm model, very high values of the R^2 correlation coefficient ($R^2 > 0.95$) were obtained indicating that this model describes the adsorption process well. The $q_{m,cal}$ values are 219.00 mg g^{-1} (AC-$1.5_{3\text{-}CO2}$) and 253.20 mg g^{-1} (AC-$2_{3\text{-}CO2}$); therefore, they are very close to the experimentally obtained $q_{e,exp}$ (Table 6). However, the average absolute percentage deviation (%Dev) is relatively high (~9%). For the Freundlich model, the values of the R^2 are slightly smaller compared to those for the Langmuir one. The K_F coefficient, which is the affinity constant indicating the strength of the interactions between the adsorbate and the adsorbent, is high for both tested materials (AC-$1.5_{3\text{-}CO2}$–48.22 and AC-$2_{3\text{-}CO2}$–57.24). The n values are ~4.2 which can indicate a significant contribution of chemical adsorption. The higher the value of n, the greater the interactions between the dye molecules and carbon [48]. Unfortunately, the %Dev is ~20% which means that there is a very large difference between the values of $q_{e,exp}$ obtained experimentally and the predicted values of $q_{e,pred}$. The models of the Langmuir and Freundlich isotherms do not explain the adsorption mechanism sufficiently.

Thus, the Radke–Prausnitz isotherm model was applied (Fig. 6c, d). As for this isotherm model, very good fitting was obtained. The correlation coefficient was $R^2 = 98$ for both tested materials. Moreover, the average absolute percentage deviation (%Dev) values were also small (AC-$1.5_{3\text{-}CO2}$–5.65% and AC-$2_{3\text{-}CO2}$–6.98%, Table 6). As a result, it was stated that this model is the most appropriate for explanation of the methylene blue adsorption mechanism. The sorption capacities of the obtained carbons were compared with those of the other materials (literature data) and are given in Table 7.
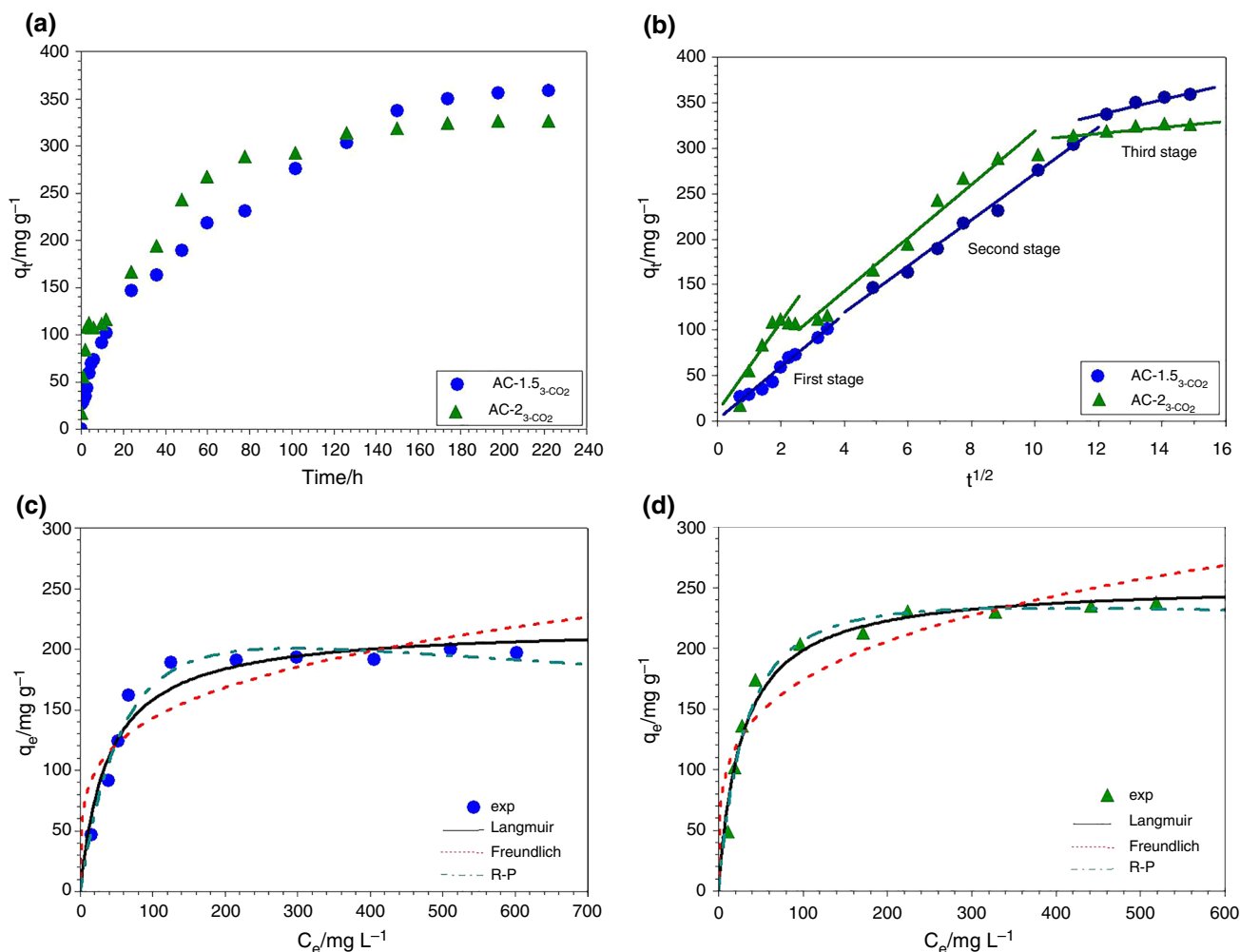
Fig. 6 Kinetics of methylene blue adsorption (**a**) and intra-particle diffusion model of the adsorption process (**b**) on the carbons AC-1.5$_{3\text{-CO2}}$ and AC-2$_{3\text{-CO2}}$ as well as the nonlinear fitting of the isotherm models for the samples: AC-1.5$_{3\text{-CO2}}$ (**c**) and AC-2$_{3\text{-CO2}}$ (**d**)

Table 5 The calculated parameters values in the linear forms of the kinetic models for the studied materials (a, b)

(a)			Pseudo-first order			Pseudo-second order			Elovich kinetic model		
Sample designation	$q_{e,exp}$	σ	$q_{e,calc}$	k_1	R^2	$q_{e,calc}$	k_2	R^2	α	β	R^2
AC-1.5$_{3\text{-CO2}}$	358.76	0.060	372.04	$4.61*10^{-2}$	0.93	500.00	$5.13*10^{-5}$	0.96	0.835	0.016	0.90
AC-2$_{3\text{-CO2}}$	311.40	0.104	244.94	$8.06*10^{-2}$	0.98	500.00	$9.3*10^{-5}$	0.99	1.667	0.018	0.94
(b)			*Intra-particle kinetic diffusion model*								
	First stage			*Second stage*			*Third stage*				
Sample designation	k_{d1}	C_1	R^2	k_{d2}	C_2	R^2	k_{d3}	C_3			R^2
AC-1.5$_{3\text{-CO2}}$	29.02	0.125	0.97	25.41	15.79	0.98	7.94	242.4			0.92
AC-2$_{3\text{-CO2}}$	50.80	0.512	0.82	29.16	23.29	0.96	3.64	273.8			0.91

$q_{e,exp}$—the amount of adsorbed substance per 1 g of adsorbent after time t (averaged values) [mg g^{-1}]; σ—the standard deviation; k_1—the pseudo-first order reaction rate constant [h^{-1}]; k_2—the pseudo-second order reaction rate constant [gmg^{-1} h^{-1}]; α—the initial adsorption rate [mg g^{-1} h^{-1}]; β—the desorption constant [g mg^{-1}]; k_{d1}, k_{d2}, k_{d3}—the intra-particle diffusion rate constant of the first, second and third stages [mg •• h$^{1/2}$ g^{-1}]; C_1, C_2, C_3—the boundary layer thickness of the first, second and third stages [mg g^{-1}]

Table 6 The calculated values of the variables in the nonlinear forms of the isotherm models used for the MB adsorption modeling

Sample designation	$q_{e, exp}$	σ	Langmuir				Freundlich				Radke–Prausnitz				
			$q_{m, calc}$	K_L	R^2	%Dev	n	K_F	R^2	%Dev	K_{RP}	α	β	R^2	%Dev
AC-1.5$_{3-CO2}$	200.30	0.070	219.00	0.026	0.96	9.32	4.24	48.22	0.87	19.56	3.74	0.004	1.22	0.98	5.65
AC-2$_{3-CO2}$	237.67	0.119	253.20	0.036	0.98	8.58	4.14	57.24	0.91	19.79	7.55	0.018	1.09	0.98	6.98

q_e—the amount of adsorbed dye per 1 g of adsorbent at equilibrium (averaged values) [mg g^{-1}]; σ—the standard deviation; K_L—the Langmuir adsorption equilibrium constant [L mg^{-1}]; K_F—the Freundlich constant which indicates the adsorption capacity [mg g^{-1}]; n—the Freundlich adsorption intensity constant; K_{RP}—the Radke–Prausnitz isotherm constant [L mg^{-1}]; α—the Radke–Prausnitz isotherm constant [L$^\beta$ mg$^{-\beta}$]; β—the Radke–Prausnitz isotherm model exponent related to the adsorption heterogeneity

Table 7 The comparison of the sorption capacity of activated carbons in relation to MB obtained from organic waste materials impregnated with H$_3$PO$_4$

Starting material	Impregnation ratio	Activation conditions	S_{BET} (m^2 g^{-1})	Adsorption capacity (mg g^{-1})	Ref.
Coffee grounds	30 mass%	450 °C–1 h /air	514	96.1	[49]
	60 mass%		618	129.9	
	120 mass%		745	163.9	
	180 mass%		925	181.8	
Mangrove pile	4	300 °C–1 h /N$_2$	1011.8	434.78	[50]
E. angustifolia seeds	–	–	1127	71.94	[51]
Eucalyptus camaldulensis Dehn bark	1:1 with 85% acid by mass	500 °C–1 h /air	1043	427	[52]
Eucalyptus residue (branches of eucalyptus)	1.0	400 °C–3 h /N$_2$	1144.56	874.05	[53]
	1.5		1237.93	912.06	
	2.0		1363.68	937.90	
Camellia oleifera shell	3:1	600 °C–1 h	1608	330	[54]
Mangosteen peel	1:3 (40% acid concentration)	450 °C–1 h/O$_2$limited	1832.3	871.49	[55]
Rice husks	4:1	500 °C–1 h /N$_2$	2028	578.0	[56]
Globe artichoke leaves	200 wt.%	500 °C–1 h /air	2038	780.0	[57]
Corncob	1.0	400 °C–1 h / Ar	2081	215.0	[58]
Almond shells	0.7:1	500 °C–45 min / N$_2$	1128	148	[59]
Canarium Odontophyllum (Dabai) Nut-shell	60 wt%	700 °C–2 h/ N$_2$	1024	333.33	[60]
Coconut leaves	4	microwave –20 min / N$_2$	631.6	250.0	[61]
Waste wood pallets	1.5 (36% acid concentration)	550 °C–1.5 h/N$_2$	1226.7	625.0	[62]
Corncob	1:2 wt%	microwave –20 min / N$_2$	415.2	183.3	[63]
Shrimp shell waste	–	500 °C–2 h/N$_2$	560.6	826.0	[64]
Spent coffee grounds	1.5	800 °C–3 h/CO$_2$	614.8	200.3	This study
	2		720.9	237.67	

Conclusions

It was proved that the use of household waste materials is an alternative way to reduce the amount of wastes and reuse them for the micro-mesoporous effective carbon adsorbents production. The analysis of surface heterogeneity using the water thermodesorption under the Q-TG conditions shows a few stages of the process at the surface/water and water/air interfaces as a result of strong interactions of water molecules inside the micropores. The formation of various water clusters on the heterogeneous surface of ACs was found. The cryoporometry tests showed a decrease in the melting temperature of ice in the pores. Taking into account the non-freezing water layer, it was stated that ACs are characterized by a narrow pore size distribution and the value of R_{dom} about 1.1 nm. The trends of intensity changes on the dV/dR curves confirm the increase in the volume of micropores with the increasing the degree of impregnation. The materials show an amorphous nature. The activated carbons are characterized by a very good sorption capacity in relation to

methylene blue ($q_{e,exp} = 200.3$–237.67 mg g^{-1}). The adsorption process proceeded according to the Radke–Prausnitz isotherm model.

Declarations

References

1. Chen D, Yin L, Wang H, He P. Pyrolysis technologies for municipal solid waste: a review. Waste Manag. 2014. https://doi.org/10.1016/j.wasman.2014.08.004.

2. Czajczyńska D, Anguilano L, Ghazal H, Krzyżyńska R, Reynolds AJ, Spencer N, Jouhara H. Potential of pyrolysis processes in the waste management sector. Therm Sci Eng Prog. 2017. https://doi.org/10.1016/j.tsep.2017.06.003.

3. Altıntıg E, Altundag H, Tuzen M, Sarı A. Effective removal of methylene blue from aqueous solutions using magnetic loaded activated carbon as novel adsorbent. Chem Eng Res Des. 2017. https://doi.org/10.1016/j.cherd.2017.03.035.

4. Altıntıg E, Onaran M, Sarı A, Altundag H, Tuzen M. Preparation, characterization and evaluation of bio-based magnetic activated carbon for effective adsorption of malachite green from aqueous solution. Mater Chem Phys. 2018. https://doi.org/10.1016/j.matchemphys.2018.05.077.

5. Zięzio M, Charmas B, Jedynak K, Hawryluk M, Kucio K. Preparation and characterization of activated carbons obtained from the waste materials impregnated with phosphoric acid (V). Appl Nanosci. 2020. https://doi.org/10.1007/s13204-020-01419-6.

6. Altıntıg E, Yenigun M, Sarı A, Altundag H, Tuzen M, Saleh TA. Facile synthesis of zinc oxide nanoparticles loaded activated carbon as an eco-friendly adsorbent for ultra-removal of malachite green from water. Environ Technol Innov. 2021. https://doi.org/10.1016/j.eti.2020.101305.

7. Varma AK, Thakur LS, Shankar R, Mondal P. Pyrolysis of wood sawdust: effects of process parameters on products yield and characterization of products. Waste Manag. 2019. https://doi.org/10.1016/j.wasman.2019.04.016.

8. Cheng F, Bayat H, Jena U, Brewer CE. Impact of feedstock composition on pyrolysis of low-cost, protein- and lignin-rich biomass: a review. J Anal Appl Pyrolysis. 2020. https://doi.org/10.1016/j.jaap.2020.104780.

9. Nahil MA, Williams PT. Activated carbons from acrylic textile waste. J Anal App Pyrolysis. 2010. https://doi.org/10.1016/j.jaap.2010.05.005.

10. Grycová B, Koutník I, Pryszcz A. Pyrolysis process for the treatment of food waste. Bioresour Technol. 2016. https://doi.org/10.1016/j.biortech.2016.07.064.

11. Giwa AS, Xu H, Wu J, Li Y, Chang F, Zhang X, Jin Z, Huang B, Wang K. Sustainable recycling of residues from the food waste (FW) composting plant via pyrolysis: thermal characterization and kinetic studies. J Clean Prod. 2018. https://doi.org/10.1016/j.jclepro.2018.01.122.

12. Paulik F, Paulik J, Arnold M. TG and TGT investigations of the decomposition of nitrocellulose under quasi-isothermal conditions. J Therm Anal Calorim. 1977. https://doi.org/10.1007/BF01909596.

13. Coats AW, Redfern JP. Thermogravimetric analysis. A review. Analyst. 1963. https://doi.org/10.1039/an963880090.

14. Kristl M, Muršec M, Šuštar V, Kristl J. Application of thermogravimetric analysis for the evaluation of organic and inorganic carbon contents in agricultural soils. J Therm Anal Calorim. 2015. https://doi.org/10.1007/s10973-015-4844-1.

15. Paulik F, Paulik J, Erdey L. Derivatography: acomplex method in thermal analysis. Talanta. 1966. https://doi.org/10.1016/0039-9140(66)80083-8.

16. Paulik F, Paulik J. Simultaneous thermogravimetric and thermo-gas-titrimetric investigations under quasi-isothermal and quasi-isobaric conditions. Anal Chim Acta. 1973. https://doi.org/10.1016/S0003-2670(01)80878-3.

17. Skinner LM, Sambles JR. The Kelvin equation—a review. J Aerosol Sci. 1972. https://doi.org/10.1016/0021-8502(72)90158-9.

18. Brun M, Lallemand A, Quinson JF, Eyraud C. A new method for the simultaneous determination of the size and shape of pores: the thermoporometry. Thermochim Acta. 1977. https://doi.org/10.1016/0040-6031(77)85122-8.

19. Riikonen J, Salonen J, Lehto VP. Utilising thermoporometry to obtain new insights into nanostructured materials. J Therm Anal Calorim. 2010. https://doi.org/10.1007/s10973-010-1167-0.

20. Landry MR. Thermoporometry by differential scanning calorimetry: experimental considerations and applications. Thermochim Acta. 2005. https://doi.org/10.1016/j.tca.2005.02.015.

21. Charmas B, Zięzio M, Tomaszewski W, Kucio K. Smart preparation of microporous carbons from spent coffee grounds. Comprehensive characterization and application in explosives removal from water samples. Colloids Surf A Physicochem Eng Asp. 2022. https://doi.org/10.1016/j.colsurfa.2022.128889.

22. Gregg SJ, Sing KSW. Adsorption, surface area and porosity. London: Academic Press; 1982.

23. Gun'ko VM, Mikhalovsky SV. Evaluation of slitlike porosity of carbon adsorbents. Carbon. 2004. https://doi.org/10.1016/j.carbon.2004.01.059.

24. Turov VV, Leboda R, Skubiszewska-Zięba J, Charmas B. Application of quasi-isothermal thermogravimetry for estimation of some properties of hydration layers in mesoporous adsorbents. Colloids Surf A Physicochem Eng Asp. 2001. https://doi.org/10.1016/S0927-7757(00)00800-1.

25. Glushko VM. Handbook in thermodynamic properties of individual substances. Moscow: Nauka; 1978.

26. Gun'ko VM, Turov VV. Nuclear magnetic resonance studies of interfacial phenomena. 1st ed. CRC Press; 2013.

27. Yamamoto T, Endo A, Inagi Y, Ohmori T, Nakaiwa M. Evaluation of thermoporometry for characterization of mesoporous materials. J Colloid Interface Sci. 2005. https://doi.org/10.1016/j.jcis.2004.10.025.

28. Zelenkova G, Zelenka T, Slovak V. Thermoporometry of porous carbon: the effect of the carbon surface chemistry on the thickness of non-freezable pore water layer (delta layer). Micropor Mesopor Mat. 2021. https://doi.org/10.1016/j.micromeso.2021.111358.

29. Ishikiriyama K, Todoki M. Pore size distribution measurements of silica gels by means from differential scanning calorimetry II. Thermoporosimetry. J Colloid Interface Sci. 1995. https://doi.org/10.1006/jcis.1995.1155.

30. Shafiq M, Alazba AA, Amin MT. Kinetic and isotherm studies of Ni^{2+} and Pb^{2+} adsorption from synthetic wastewater using *Eucalyptus camdulensis*—derived biochar. Sustainability. 2021. https://doi.org/10.3390/su13073785.

31. Palanivell P, Ahmed OH, Latifah O, Majid NMA. Adsorption and desorption of nitrogen, phosphorus, potassium, and soil buffering capacity following application of chicken litter biochar to an acid soil. Appl Sci. 2020. https://doi.org/10.3390/app10010295.

32. Rigueto CVT, Piccin JS, Dettmer A, Rosseto M, Dotto GL, de Oliveira Schmitz AP, Perondi D, Martins de Freitas TS, Loss RA, Geraldi CAQ. Water hyacinth (*Eichhornia crassipes*) roots, an amazon natural waste, as an alternative biosorbent to uptake a reactive textile dye from aqueous solutions. Ecol Eng. 2020. https://doi.org/10.1016/j.ecoleng.2020.105817.

33. Gao J, Wang T, Shu Q, Nawaz Z, Wen Q, Wang D, Wang J. An adsorption kinetic model for sulfur dioxide adsorption by ZL50 activated carbon. Chin J Chem Eng. 2010. https://doi.org/10.1016/S1004-9541(08)60346-8.

34. Unger KK, Rouquerol J, Sing KSW. Eds. Characterization of porous solids, proceedings of the IUPAC symposium (COPSI). 1st ed. Elsevier: Amsterdam, Oxford, New York, Tokyo; 1988.

35. Gun'ko VM, Savina IN, Mikhalovsky SV. Cryogels: morphological, structural and adsorption characterization. Adv Colloid. 2013. https://doi.org/10.1016/j.cis.2012.11.001.

36. Staszczuk P, Dobrowolski R, Jaroniec M. Investigations of water film on the surface of activated carbon by thermal analysis. Langmuir. 1992. https://doi.org/10.1021/la00037a042.

37. Charmas B, Kucio K, Sydorchuk V, Khalameida S, Zięzio M, Nowicka A. Characterization of multimodal silicas using TG/DTG/DTA Q-TG and DSC methods. 2019. Colloid Interfaces. https://doi.org/10.3390/colloids3010006.

38. Shimodaira N, Masui A. Raman spectroscopic investigations of activated carbon materials. J Appl Phys. 2002. https://doi.org/10.1063/1.1487434.

39. Blankenship TS, Balahmar N, Mokaya R. Oxygen-rich microporous carbons with exceptional hydrogen storage capacity. Nat Commun. 2017. https://doi.org/10.1038/s41467-017-01633-x.

40. Ferrari AC, Robertson J. Interpretation of Raman spectra of disordered and amorphous carbon. Phys Rev B. 2000. https://doi.org/10.1103/PhysRevB.61.14095.

41. Alcaraz L, Escudero ME, Alguacil FJ, Llorente I, Urbieta A, Fernández P, López FA. Dysprosium removal from water using active carbons obtained from spent coffee ground. Nanomaterials. 2019. https://doi.org/10.20944/preprints201908.0076.v1.

42. Sahoo TR, Prelot B. Adsorption processes for the removal of contaminants from wastewater: the perspective role of nanomaterials and nanotechnology. In: Nanomaterials for the detection and removal of wastewater pollutants, Elsevier 2020; https://doi.org/10.1016/B978-0-12-818489-9.00007-4.

43. Wu FC, Tseng RL, Juang RS. Characteristics of Elovich equation used for the analysis of adsorption kinetics in dye-chitosan systems. Chem Eng J. 2009. https://doi.org/10.1016/j.cej.2009.01.014.

44. Cheung WH, Szeto YS, McKay G. Intraparticle diffusion processes during acid dye adsorption onto chitosan. Bioresour Technol. 2007. https://doi.org/10.1016/j.biortech.2006.09.045.

45. Campos NF, Barbosa CM, Rodríguez-Díaz JM, Duarte MM. Removal of naphthenic acids using activated charcoal: kinetic and equilibrium studies. Adsorp Sci Technol. 2018. https://doi.org/10.1177/0263617418773844.

46. Cheng CS, Deng J, Lei B, He A, Zhang X, Ma L, Li S, Zhao C. Toward 3D graphene oxide gels based adsorbents for high-efficient water treatment via the promotion of biopolymers. J Hazard Mater. 2013. https://doi.org/10.1016/j.jhazmat.2013.09.065.

47. Puziy AM, Poddubnaya OI, Socha RP, Gurgul J, Wiśniewski M. XPS and NMR studies of phosphoric acid activated carbons. Carbon. 2008. https://doi.org/10.1016/j.carbon.2008.09.010.

48. Sahu S, Pahi S, Tripathy S, Singh SK, Behera A, Sahu UK, Patel RK. Adsorption of methylene blue on chemically modified lychee seed biochar: dynamic, equilibrium, and thermodynamic study. J Mol Liq. 2020. https://doi.org/10.1016/j.molliq.2020.113743.

49. Reffas A, Bernardet V, David B, Reinert L, Lehocine MB, Dubois M, Batisse N, Duclaux L. Carbons prepared from coffee grounds by H_3PO_4 activation: characterization and adsorption of methylene blue and nylosan red N-2RBL. J Hazard Mater. 2010. https://doi.org/10.1016/j.jhazmat.2009.10.076.

50. Zakaria R, Jamalluddin NA, Bakar MZA. Effect of impregnation ratio and activation temperature on the yield and adsorption performance of mangrove based activated carbon for methylene blue removal. Res Mater. 2021. https://doi.org/10.1016/j.rinma.2021.100183.

51. Baytar O, Ceyhan AA, Şahin Ö. Production of activated carbon from *Elaeagnus angustifolia* seeds using H_3PO_4 activator and methylene blue and malachite green adsorption. Int J Phytoremediation. 2020. https://doi.org/10.1080/15226514.2020.1849015.

52. Patnukao P, Pavasant P. Activated carbon from Eucalyptus camaldulensis Dehn bark using phosphoric acid activation. Bioresour Technol. 2008. https://doi.org/10.1016/j.biortech.2006.10.049.

53. Han Q, Wang J, Goodman BA, Xie J, Liu Z. High adsorption of methylene blue by activated carbon prepared from phosphoric acid treated eucalyptus residua. Powder Technol. 2020. https://doi.org/10.1016/j.powtec.2020.02.013.

54. Kang S, Jian-chun J, Dan-dan C. Preparation of activated carbon with highly developer mesoporous structure from Camellia oleifera shell through water vapor gasification and phosphoric acid modification. Biomass Bioener. 2011. https://doi.org/10.1016/j.biombioe.2011.05.007.

55. Zhang Z, Xu L, Liu Y, Feng R, Zou T, Zhang Y, Kang Y, Zhou P. Efficient removal of methylene blue using the mesoporous activated carbon obtained from mangosteen peel wastes: kinetic, equilibrium, and thermodynamic studies. Micropor Mesopor Mat. 2021. https://doi.org/10.1016/j.micromeso.2021.110904.

56. Chen Y, Zhai SR, Liu N, Song Y, An QD, Song XW. Dye removal of activated carbons prepared from NaOH-pretreated rice husks by low-temperature solution-processed carbonization and H_3PO_4 activation. Bioresour Technol. 2013. https://doi.org/10.1016/j.biortech.2013.07.002.

57. Benadjemia M, Millière L, Reinert L, Benderdouche N, Duclaux L. Preparation, characterization and methylene blue adsorption of phosphoric acid activated carbons from globe artichoke

leaves. Fuel Process Technol. 2011. https://doi.org/10.1016/j.fuproc.2011.01.014.

58. Sych NV, Trofymenko SI, Poddubnaya OI, Tsyba MM, Sapsay VI, Klymchuk DO, Puziy AM. Porous structure and surface chemistry of phosphoric acid activated carbon from corncob. Appl Surf Sci. 2012. https://doi.org/10.1016/j.apsusc.2012.07.084.

59. İzgi MS, Saka C, Baytar O, Saraçoğlu G, Şahin Ö. Preparation and characterization of activated carbon from microwave and conventional heated almond shells using phosphoric acid activation. Anal Lett. 2019. https://doi.org/10.1080/00032719.2018.1495223.

60. Vicinisvarri I, Kumar SS, Aimi N, Norain I, Izza N. Preparation and characterization of phosphoric acid activated carbon from *Canarium Odontophyllum* (Dabai) nutshell for methylene blue adsorption. Res J Chem Environ. 2014;18:57–62.

61. Jawad AH, Sabar S, Ishak MAM, Wilson LD, Norrahma SSA, Talari MK, Farhan AM. Microwave-assisted preparation of mesoporous activated carbon from coconut (*Cocos Nucifera*) leaf by H_3PO_4-activation for methylene blue adsorption. Chem Eng Commun. 2017. https://doi.org/10.1080/00986445.2017.1347565.

62. Tsang DCW, Hu J, Liu MY, Zhang W, Lai KCK, Lo IMC. Activated carbon produced from waste wood pallets: adsorption of three classes of dyes. Water Air Soil Pollut. 2007. https://doi.org/10.1007/s11270-007-9404-2.

63. Jawad AH, Bardhan M, Islam MA, Islam MA, Syed-Hassan SSA, Surip SN, ALOthman ZA, Khan MR. Insights into the modeling, characterization and adsorption performance of mesoporous activated carbon from corn cob residue via microwave-assisted H_3PO_4 activation. Surf Interfaces. 2020. https://doi.org/10.1016/j.surfin.2020.100688.

64. Liu X, He C, Yu X, Bai Y, Ye L, Wang B, Zhang L. Net-like porous activated carbon materials from shrimp shell by solution-processed carbonization and H_3PO_4 activation for methylene blue adsorption. Powder Technol. 2018. https://doi.org/10.1016/j.powtec.2017.12.034.